RESEARCH ARTICLE-MECHANICAL ENGINEERING

A Novel Smooth Super-Twisting Control Method for Perturbed Nonlinear Double-Pendulum-Type Overhead Cranes

Muhammad A. Shehu[1] · Aijun Li[1]

Abstract

The double-pendulum (DP) phenomenon, effectuated by the fact that the payload configuration and the chain length between the hook and the payload are usually unknown, is a typical issue in actual cranes. This phenomenon is considered in the current study to enhance tracking accuracy and sway regulation for overhead cranes subject to perturbations and multiple frictions. A novel smooth super-twisting algorithm hybridized with the integral sliding mode control (ISMC) is proposed to solve the problems. The closed-loop system's finite time stability has been examined using a strict quadratic Lyapunov function. Compared to an existing modified super-twisting algorithm (MSTC), it has been shown that the proposed algorithm mitigates both the sliding surface overshoot and the initial peaking of the control effort that can be encountered using the MSTC algorithm. Furthermore, simulation experiments and error analysis show improved effectiveness of the proposed technology against the existing MSTC and the conventional ISMC technologies. The paper contribution primarily dwells on devising a novel structure of super-twisting algorithm that ensures the nonlinear perturbed DP overhead crane's desired performance.

Keywords Under-actuated mechanical systems · Super-twisting control · Lyapunov · Double-pendulum cranes

1 Introduction

The overhead crane is an indispensable manipulation system. It offers heavy cargo transportation services in areas such as the transportation sector, automated assembly lines, shipping yards, automotive industries, mining sector, power plants, and marine industries. Traditionally, the crane is controlled manually. However, due to the human operator's incompetence in handling the crane, flexibility of the system, and the presence of unexpected endogenous and exogenous disturbances, it may suffer from excessive payload sway. Thus, crane manufacturers devote colossal efforts to build fully automated cranes that meet particular safety and performance criteria. Besides the effects of extraneous perturbations (such as winds, collisions), the hoisting rope's flexibility makes the system lightly damped. Thus, the trolley motion induces undesirable oscillations that make fast and precise payload

positioning time-consuming. Additionally, its operation may even be risky, especially when the payload is of a hazardous type. It should be understood that the crane system is highly nonlinear, under-actuated (primarily when DP phenomenon exists). Stabilization of under-actuated mechanical systems is challenging since it is difficult to evaluate the complex nonlinear behaviour of the uncontrolled dynamics with traditional analysis methods [1–3].

As control scheme developments have progressed, efforts have been devoted to the control of under-actuated overhead cranes in recent decades [4–31]. The similarity in these works is that they all consider the payload's sway as a simple pendulum. That is, compared with the payload, the hook's mass is wholly ignored. Additionally, the payload is treated as a point mass. However, in practical operations, the payload size is usually large, and the hook mass cannot be neglected. Consequently, as the trolley accelerates/decelerates, the hook oscillates around the trolley. The payload oscillates around the hook simultaneously, producing rather complex DP swing dynamics. The appearance of DP effects further complicates the control problem due to the increased under-actuation degree. Furthermore, the system dynamics are entirely different, consequently deteriorating the performances of traditional control algorithms that are

✉ Muhammad A. Shehu
  shehu.muhammad@mail.nwpu.edu.cn

  Aijun Li
  liaijun@nwpu.edu.cn

[1] School of Automation, Northwestern Polytechnical University, Xi'an 710072, Shaanxi, China

developed without considering the DP effects. Hence, considering this common scenario in real-world applications alongside the effects of parasitic dynamics, nonzero initial conditions, frictions, and external disturbances (such as noise and wind), the effectiveness of the proposed feed-forward techniques such as [7–13] may not always be reliable since they are susceptible to perturbations. That being said, the merits of these techniques, such as design simplicity (since no feedback sensors are required), cannot be suppressed. On the other hand, the effectiveness of the proposed classical feedback control algorithms, such as pole placement [14], proportional integral derivative control [15–17], linear quadratic regulator [18], and model predictive control [19], designed using small-angle approximation is limited to the closeness of this approximation to the real crane system.

A feedback strategy observed to be the most robust in dealing with uncertainties and external disturbances for single-pendulum cranes is the sliding mode control (SMC) [20–36]. The SMC is a variable structure control system characterized by a discontinuous control structure that switches as the system crosses a specific *manifold* in the state space. It drives the system trajectory to *reach* and subsequently *slide* along the manifold along which the system is entirely insensitive to the so-called *matched* perturbations. However, during this transient *reaching* phase, the tracking error is difficult to control since the *sliding mode* is yet to be reached, and the crane may be sensitive to perturbations. One would ideally like to shorten the reaching duration or even eliminate it. One easy way to shorten the reaching duration is to employ more considerable control gains. Using higher gains could increase robustness when one is dealing with large perturbations. However, using higher gains may result in extreme crane sensitivity to parasitic dynamics, actuator saturation, and higher unwanted chattering (a well-known drawback of first-order SMC). It is worth noting that the switching gain should be small for SMC to be practically realizable. Nevertheless, small gains may result in SMC's performance degradation. Nevertheless, small gains may result in SMC's performance degradation. To eliminate the reaching phase for cranes with actuator nonlinearities, Defoort et al. [31] proposed a control solution based on integral SMC (ISMC). To circumvent the unwanted chattering, second-order twisting control was proposed by [29]. However, the use of twisting algorithms increases design complexity since the sliding variable's time derivative is needed. To improve robustness to perturbations, have finite time convergence, and suppress the chattering without the need of sliding variable time derivative, the most preferred second-order SMC algorithm is the super-twisting control (STC) [37].

Considering the highlighted DP problem in actual cranes, it is crucial to design an effective controller that considers the DP effects. Regarding this DP topic, fewer works on SMC were reported in the literature compared to those for traditional single-pendulum cranes, for instance, in [38–41]. The majority of the available control algorithms for DP cranes are using nonlinear Lyapunov-based energy methods [42–48] with complex control algorithms. Elsewhere, the PID [49] and feed-forward strategies like input shaping technique [50–52] and trajectory planning techniques (TP) [53,54] have been proposed. Although input shaping technology or other trajectory planning control techniques have been used to tackle the DP problem in cranes and good results achieved, as classic feed-forward control techniques, they primarily rely on the crane's linear model. Input shaping only deals with sway suppression of the payload, neglecting the positioning accuracy and trolley speed. Elsewhere, in TP control, the crane trajectory planning problem is not fully solved yet, but only provides reasonable solutions for many practical problems. More so, using these feed-forward methods, the control effectiveness might deteriorate when external disturbance or parameter variations occurred. Hence, it is needed to include state feedback into the control strategy for better robustness.

Many studies were without simultaneous regards to the DP effect (a common scenario in practice due to large hook mass or irregular payload), friction, model uncertainties, and disturbances. However, these perturbations' effects could induce DP effects and positioning error in practice, increasing the difficulty to guarantee control effectiveness. Concerning the highlighted research gap, these problems are simultaneously considered in this paper to work with a more practical crane case. Also, an event that occurs in practice is that when the target position is issued to the controller, the initial control effort may be enormous to overdrive the trolley. In this work, a novel smooth super-twisting control algorithm (NSSTC) is proposed. We will show that using the proposed NSSTC algorithm, the initial peaking of the control effort and the overshoot in the sliding surface variable that may be obtained using a recently proposed modified super-twisting algorithms (MSTC) in [55] and [56] may be alleviated. Additionally, the proposed NSSTC technique can achieve some superior performance than the MSTC technique. The stability of the closed-loop system is proved using a strict quadratic Lyapunov function. Lastly, the effectiveness of the proposed control technique is demonstrated by numerical simulations and tracking error analysis.

The paper's contribution is summarized as follows.

(1) The mathematical model of a perturbed overhead crane that considers the DP effect, actuator dynamics, and friction is presented.
(2) The paper proposes a hybrid control strategy using ISMC and novel smooth super-twisting control (NSSTC) for position tracking and sway regulation for DP cranes.
(3) It will be shown that the novel algorithm mitigates the sliding surface overshoot and the initial peaking of the

control effort, as well as improved performance compared to the MSTC algorithm.

(4) To our best knowledge, it will be the first time the algorithm is tested on overhead cranes subject to DP effect, parasitic dynamics, disturbances, and various frictions. To our best knowledge, few works have been reported in control of these effects simultaneously.

(5) The proposed algorithm is simple, and sufficient closed-loop stability analysis is proved, implying the proposed algorithm's effectiveness.

In this paper, $\Re$, $\Re^+$, and $\Re^n$ refer to the spaces of real numbers, positive real numbers, and real n-vectors, respectively. $\|\mathbf{X}\|$ is the *Frobenius norm* of $\mathbf{X}$, σ is a stable manifold in space with boundary ω, while $x \in \Re$, $r \in \Re^+$, $\mathbf{X} \in \Re^n$, and n is a natural number.

Paper organization is as follows. Section 2 presents the model of the nominal and perturbed overhead crane. Section 3 is devoted to the design of the proposed NSSTC-ISMC hybrid strategy and the stability analysis of the closed-loop system from a mathematical perspective. In Sect. 4, control experiments, performance evaluation, and comparative analysis of the obtained results based on mean absolute error (MAE) and mean squared error (MSE) criteria are presented. Section 5 concludes the paper.

2 Problem Formulation

2.1 Nominal Crane Dynamics

The schematic diagram of the system under study is shown in Fig. 1: a three-degree-of-freedom, 2D overhead crane. The parameters of the system are defined in Table 1. Derivation of the model of the overhead crane system is based on the Euler–Lagrange method. For simplicity, the following assumptions are considered: (1) hoisting cable is massless; (2) all joints are well lubricated; (3) hoisting is only needed for obstacle avoidance; and (4) information about the mass of the payload, cart position, payload and hook sways, and hoisting height is available through sensors.

By defining independent generalized coordinates as $\mathbf{q} \triangleq \begin{bmatrix} q_1 & q_2 & q_3 \end{bmatrix}^{\mathrm{T}} = \begin{bmatrix} x & \theta_{\mathrm{h}} & \theta_{\mathrm{p}} \end{bmatrix}^{\mathrm{T}}$, and non-conservative forces as $\mathbf{Q}_{\mathrm{c}} \triangleq \begin{bmatrix} Q_1 & Q_2 & Q_3 \end{bmatrix}^{\mathrm{T}} = \begin{bmatrix} F_{\mathrm{c}} & 0 & 0 \end{bmatrix}^{\mathrm{T}}$, using the Euler–Lagrange method, the system's equations of motion (EOM) can easily be obtained in matrix compact as

$$\mathbf{M}_{\mathrm{c}}(\mathbf{q})\ddot{\mathbf{q}} + \mathbf{C}_{\mathrm{c}}(\mathbf{q}, \dot{\mathbf{q}})\dot{\mathbf{q}} + \mathbf{G}_{\mathrm{c}}(\mathbf{q}) = \mathbf{Q}_{\mathrm{c}}; \qquad (1)$$

where the acceleration-related inertia matrix $\mathbf{M}_{\mathrm{c}}(\mathbf{q}) \in \Re^{3 \times 3}$, the velocity-related *Coriolis–centrifugal* matrix $\mathbf{C}_{\mathrm{c}}(\mathbf{q}, \dot{\mathbf{q}}) \in \Re^{3 \times 3}$, and the gravity vector $\mathbf{G}_{\mathrm{c}}(\mathbf{q}) \in \Re^3$ are defined as:

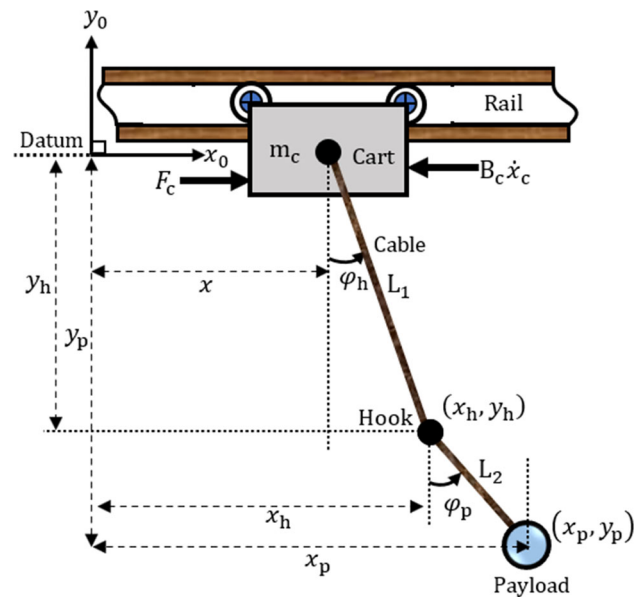**Fig. 1** Overhead crane schematic diagram

Table 1 Model parameters and variables

Notation	Description	Unit
m_{c}	Mass of travelling cart	kg
m_{p}	Mass of payload	kg
m_{h}	Mass of hook	kg
L_1	Length between cart and hook	m
L_2	Length between hook and payload	m
θ_{h}	Hook's sway angle	rad
θ_{p}	Payload's sway angle	rad
$\dot{\theta}_{\mathrm{h}}$	Hook's sway angular velocity	rad/s
$\dot{\theta}_{\mathrm{p}}$	Payload's sway angular velocity	rad/s
x	Horizontal position of cart from datum	m
$\dot{x}$	Linear velocity of travelling cart	m/s
F_{c}	Cart's physical driving force	N
F_{f}	Cart's frictional force	N
g	Acceleration by gravity	m/s²
r_{p}	Radius of travelling cart's pulley	m
R	DC motor electrical resistance	Ω
T_{m}	DC motor torque	Nm
K_{m}	DC motor torque constant	Nm/A
K_{E}	DC motor electrical constant	V/rad/s
V_{DC}	DC motor input voltage	V

$$\mathbf{M}_{\mathrm{c}}(\mathbf{q}) = \begin{bmatrix} M_{\mathrm{chp}} & M_{\mathrm{hp}}L_1\cos\theta_{\mathrm{h}} & m_{\mathrm{p}}L_2\cos\theta_{\mathrm{p}} \\ M_{\mathrm{hp}}L_1\cos\theta_{\mathrm{h}} & M_{\mathrm{hp}}L_1^2 & m_{\mathrm{p}}L_1L_2\cos\theta_{\mathrm{hp}} \\ m_{\mathrm{p}}L_2\cos\theta_{\mathrm{p}} & m_{\mathrm{p}}L_1L_2\cos\theta_{\mathrm{hp}} & m_{\mathrm{p}}L_2^2 \end{bmatrix};$$

$$\mathbf{C}_{\mathrm{c}}(\mathbf{q}, \dot{\mathbf{q}}) = \begin{bmatrix} 0 & -M_{\mathrm{chp}}L_1\dot{\theta}_{\mathrm{h}}\sin\theta_{\mathrm{h}} & -m_{\mathrm{p}}L_2\dot{\theta}_{\mathrm{p}}\sin\theta_{\mathrm{p}} \\ 0 & 0 & m_{\mathrm{p}}L_1L_2\dot{\theta}_{\mathrm{p}}\sin\theta_{\mathrm{hp}} \\ 0 & -m_{\mathrm{p}}L_1L_2\dot{\theta}_{\mathrm{h}}\sin\theta_{\mathrm{hp}} & 0 \end{bmatrix};$$

$$\mathbf{G}_{\mathrm{c}}(\mathbf{q}) = \begin{bmatrix} 0 & M_{\mathrm{chp}}gL_1\sin\theta_{\mathrm{h}} & m_{\mathrm{p}}gL_2\sin\theta_{\mathrm{p}} \end{bmatrix}^{\mathrm{T}};$$

where $M_{\mathrm{chp}} = (m_{\mathrm{c}} + m_{\mathrm{h}} + m_{\mathrm{p}})$, $M_{\mathrm{hp}} = (m_{\mathrm{h}} + m_{\mathrm{p}})$ and $\theta_{\mathrm{hp}} = (\theta_{\mathrm{h}} - \theta_{\mathrm{p}})$.

A form more suitable for control design is to separate the EOM into actuated and non-actuated subsystems. Isolating $\ddot{x}$, $\ddot{\theta}_{\mathrm{h}}$ and $\ddot{\theta}_{\mathrm{p}}$ from (1) and using the notation $\mathbf{X} = \begin{bmatrix} x_1 \ x_2 \ x_3 \ x_4 \ x_5 \ x_6 \end{bmatrix}^{\mathrm{T}}$, where $x_1 = x$, $x_2 = \dot{x}$, $x_3 = \theta_{\mathrm{h}}$, $x_4 = \dot{\theta}_{\mathrm{h}}$, $x_5 = \theta_{\mathrm{p}}$ and $x_6 = \dot{\theta}_{\mathrm{p}}$. The state-space representation for the nominal crane model is obtained as:

$$\begin{cases} \dot{x}_1 = x_2; \\ \dot{x}_2 = g_1(\mathbf{X}) + b_1(\mathbf{X}) F_{\mathrm{c}}; \\ \dot{x}_3 = x_4; \\ \dot{x}_4 = g_2(\mathbf{X}) + b_2(\mathbf{X}) F_{\mathrm{c}}; \\ \dot{x}_5 = x_6; \\ \dot{x}_6 = g_3(\mathbf{X}) + b_3(\mathbf{X}) F_{\mathrm{c}}. \end{cases} \quad (2)$$

In (2), $g_i(\mathbf{X})$ and $b_i(\mathbf{X})$ are smooth nonlinear functions of the state vector $\mathbf{X}$, given by $g_i(\mathbf{X}) = G_i(\mathbf{X})/D(\mathbf{X})$ and $b_i(\mathbf{X}) = B_i(\mathbf{X})/D(\mathbf{X})$. After dropping the state dependency notations, $G_i(\mathbf{X})$, $B_i(\mathbf{X})$ and $D(\mathbf{X})$, $(i = 1, 2, 3)$ are, respectively, defined as:

$$\begin{aligned} G_1 =& [M_{\mathrm{hp}} m_{\mathrm{p}} L_1^2 L_2^2 - m_{\mathrm{p}}^2 L_1^2 L_2^2 \cos^2 x_{35}][M_{\mathrm{hp}} L_1 x_4^2 \sin x_3 \\ &+ m_{\mathrm{p}} L_2 x_6^2 \sin x_5] + [M_{\mathrm{hp}} m_{\mathrm{p}} L_1 L_2^2 \cos x_3 - m_{\mathrm{p}}^2 L_1 L_2^2 \\ &\times \cos x_5 \cos x_{35}][m_{\mathrm{p}} L_1 L_2 x_6^2 \sin x_{35} + M_{\mathrm{hp}} g L_1 \sin x_3] \\ &+ [M_{\mathrm{hp}} m_{\mathrm{p}} L_1^2 L_2 \cos x_5 - m_{\mathrm{p}} L_1^2 L_2 \cos x_3 \cos x_{35}] \\ &\times [m_{\mathrm{p}} g L_2 \sin x_5 - m_{\mathrm{p}} L_1 L_2 x_4^2 \sin x_{35}]; \end{aligned}$$

$$\begin{aligned} G_2 =& [m_{\mathrm{p}}^2 L_1 L_2^2 \cos x_5 \cos x_{35} - M_{\mathrm{hp}} m_{\mathrm{p}} L_1 L_2^2 \cos x_3][M_{\mathrm{hp}} L_1 x_4^2 \\ &\times \sin x_3 + m_{\mathrm{p}} L_2 x_6^2 \sin x_5] + [m_{\mathrm{p}}^2 L_2^2 \cos^2 x_5 - M_{\mathrm{thp}} m_{\mathrm{p}} \\ &\times L_2^2][m_{\mathrm{p}} L_1 L_2 x_6^2 \sin x_{35} + M_{\mathrm{hp}} g L_1 \sin x_3] + M_{\mathrm{thp}} m_{\mathrm{p}} \\ &\times L_1 L_2 \cos x_{35} - M_{\mathrm{hp}} m_{\mathrm{p}} L_1 L_2 \cos x_3 \cos x_5][m_{\mathrm{p}} g L_2 \\ &\times \sin x_5 - m_{\mathrm{p}} L_1 L_2 x_4^2 \sin x_{35})]; \end{aligned}$$

$$\begin{aligned} G_3 =& [M_{\mathrm{hp}} m_{\mathrm{p}} L_1^2 L_2 (\cos x_3 \cos x_{35} - \cos x_5)][M_{\mathrm{hp}} L_1 x_4^2 \sin x_3 \\ &+ m_{\mathrm{p}} L_2 x_6^2 \sin x_5] + [M_{\mathrm{thp}} m_{\mathrm{p}} L_1 L_2 \cos x_{35} - M_{\mathrm{hp}} m_{\mathrm{p}} \\ &\times L_1 L_2 \cos x_3 \cos x_5][m_{\mathrm{p}} L_1 L_2 x_6^2 \sin x_{35} + M_{\mathrm{hp}} g L_1 \sin x_3] \\ &+ [M_{\mathrm{hp}}^2 L_1^2 \cos^2 x_3 - M_{\mathrm{thp}} M_{\mathrm{hp}} L_1^2][m_{\mathrm{p}} g L_2 \sin x_5 \\ &- m_{\mathrm{p}} L_1 L_2 x_4^2 \sin x_{35}]; \end{aligned}$$

$$B_1 = M_{\mathrm{hp}} m_{\mathrm{p}} L_1^2 L_2^2 - m_{\mathrm{p}}^2 L_1^2 L_2^2 \cos^2 x_{35};$$

$$B_2 = m_{\mathrm{p}}^2 L_1^2 L_2^2 \cos x_5 \cos x_{35} - M_{\mathrm{hp}} m_{\mathrm{p}} L_1 L_2^2 \cos x_3;$$

$$B_3 = M_{\mathrm{hp}} m_{\mathrm{p}} L_1^2 L_2 \cos x_3 \cos x_{35} - M_{\mathrm{hp}} m_{\mathrm{p}} L_1^2 L_2 \cos x_5;$$

$$\begin{aligned} D =& M_{\mathrm{hp}} m_{\mathrm{p}} L_1^2 L_2^2 [M_{\mathrm{thp}} - M_{\mathrm{hp}} \cos^2 x_3] - m_{\mathrm{p}}^2 L_1^2 L_2^2 [M_{\mathrm{hp}} \\ &\times \cos^2 x_5 + M_{\mathrm{thp}} \cos^2 x_{35} - 2 M_{\mathrm{hp}} \cos x_3 \cos x_5 \cos x_{35}]; \end{aligned}$$

where $x_{35} = x_3 - x_5 = \theta_{\mathrm{h}} - \theta_{\mathrm{p}}$.

2.2 Perturbed Crane Dynamics

In practice, cranes are with un-modelled dynamics, various frictions, and external disturbances. When matched and unmatched uncertainties are considered, the uncertain system can be represented as:

$$\begin{cases} \dot{x}_1 = x_2; \\ \dot{x}_2 = \{g_1(\mathbf{X}) + \delta g_1(\mathbf{X})\} + \{b_1(\mathbf{X}) + \delta b_1(\mathbf{X})\} F_{\mathrm{c}}' + \Delta_1(\mathbf{X}); \\ \dot{x}_3 = x_4; \\ \dot{x}_4 = \{g_2(\mathbf{X}) + \delta g_2(\mathbf{X})\} + \{b_2(\mathbf{X}) + \delta b_2(\mathbf{X})\} F_{\mathrm{c}}' + \Delta_2(\mathbf{X}); \\ \dot{x}_5 = x_6; \\ \dot{x}_6 = \{g_3(\mathbf{X}) + \delta g_3(\mathbf{X})\} + \{b_3(\mathbf{X}) + \delta b_3(\mathbf{X})\} F_{\mathrm{c}}' + \Delta_3(\mathbf{X}). \end{cases} \quad (3)$$

The terms $\delta g_i(\mathbf{X})$ and $\delta b_i(\mathbf{X})$ $(i = 1, 2, 3)$ depict matched uncertainties due to parametric variations, unmodelled dynamics, neglected nonlinearities, and external disturbances. The so-called matched uncertainties mean that the perturbations $\delta g_{i0}(\mathbf{X}), \delta b_{i0}(\mathbf{X}) \in \mathrm{span}\{b_i(\mathbf{X})\}$; and enter the same channel as the control F_{c}. This statement can be explicitly expressed as:

$$\begin{cases} \delta g_i(\mathbf{X}) = b_i(\mathbf{X}) \delta \tilde{g}_i(\mathbf{X}); \\ \delta b_i(\mathbf{X}) = b_i(\mathbf{X}) \delta \tilde{b}_i(\mathbf{X}). \end{cases} \quad (4)$$

On the other hand, the terms $\Delta_i(\mathbf{X})$ $(i = 1, 2, 3)$ depict unmatched uncertainties (due to friction, measurement noise, for example) and can be expressed as:

$$\Delta_i(\mathbf{X}) = \Delta g_i(\mathbf{X}) + \Delta b_i(\mathbf{X}). \quad (5)$$

Moreover, $F_{\mathrm{c}}' = F_{\mathrm{c}} - F_{\mathrm{f}}$, where F_{f} denotes the trolley friction along x-axis that opposes the trolley force F_{c}. When (4) and (5) apply, in (3) we have the following modifications:

$$\begin{aligned} \dot{x}_{2i} =& g_i(\mathbf{X}) + b_i(\mathbf{X}) \left[\delta g_i(\mathbf{X}) + \delta \tilde{b}_i(\mathbf{X}) F_{\mathrm{c}}' + F_{\mathrm{c}}' \right] \\ &+ [\Delta g_i(\mathbf{X}) + \Delta b_i(\mathbf{X})], \quad (i = 1, 2, 3). \end{aligned} \quad (6)$$

In practice, friction model parameter identification is not trivial. Also, traditional discontinuous friction models like [57] may not be suitable for smooth control efforts. Since using discontinuous models in the analysis is rather challenging, this study adopted a recently developed continuously differentiable model given as [58]:

$$F_{\mathrm{f}} = \alpha_1 (\tanh(\beta_1 \dot{x}) - \tanh(\beta_2 \dot{x})) + \alpha_2 \tanh(\beta_3 \dot{x}) + \alpha_3 \dot{x}; \quad (7)$$

where $\alpha_1, \alpha_2, \alpha_3, \beta_1, \beta_2$, and β_3 are positive constants. In (7), the terms $[\tanh(\beta_1 \dot{x}) - \tanh(\beta_2 \dot{x})]$ captured *Stribeck friction*, the term $\alpha_2 \tanh(\beta_3 \dot{x})$ captured *Coulomb friction*, $\alpha_3 \dot{x}$ captured *Viscous friction*, while α_1 and α_2 are *stiction friction* coefficients. By selecting $\alpha_1 = 3.9$, $\alpha_2 = 2.2$, $\alpha_3 = 0.15$, $\beta_1 = 50$, $\beta_2 = 0.9$, and $\beta_3 = 70$, the friction uncertainties described by the model (7) are as shown in Fig. 2.

Remark 1 In practice, the payload is always suspended below the trolley; hence, $L_1 \in \Re^+$ and $L_2 \in \Re^+$, $\forall t$. Moreover,
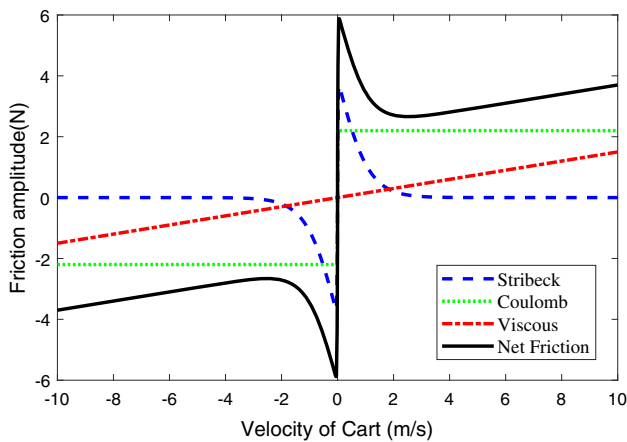
Fig. 2 Friction uncertainty profile

for safe operation, sway angles θ_h and θ_p satisfy the range $-\frac{\pi}{2} < (\theta_h, \theta_p) < \frac{\pi}{2}, \forall t$.

The below assumptions will be invoked for the design and stability analysis of the control system presented in Sect. 3.

Assumption 1 The drifting terms, $g_i(\mathbf{X})$; and the control channel terms, $b_i(\mathbf{X})$; for $i = 1, 2, 3$, are smooth nonlinear functions. Additionally, along Remark 1, the terms $b_i(\mathbf{X})$, are invertible $\forall \mathbf{X}$.

Assumption 2 The uncertainties are Lipschitz continuous and bounded such that $|\delta \tilde{g}_i(\mathbf{X})| \leq \delta_g$, $|\delta \tilde{b}_i(\mathbf{X})| \leq \delta_b$, $|\Delta g_i(\mathbf{X})| \leq \Delta_g$ and $|\Delta b_i(\mathbf{X})| \leq \Delta_b$, $(i = 1, 2, 3)$, where $\delta_g \in \Re^+$, $\delta_b \in \Re^+$, $\Delta_g \in \Re^+$, and $\Delta_b \in \Re^+$ are known upper bounds.

2.3 DC Actuator Dynamics

Since the cart's physical force (F_c), in (2) is generated by a DC motor, actuator dynamic is taken into account. The following equation set relates the linear force, F_c; with motor torque, T_m; and motor input voltage, V_{DC}:

$$\begin{cases} T_m = r_p F_c = \frac{K_m}{R} V_{DC} - \frac{K_m K_E}{R} \omega_m; \\ \omega_m = \frac{x_2}{r_p}, \end{cases} \tag{8}$$

where r_p, K_m, V_{DC}, K_E, and R have been earlier defined in Table 1, while ω_m is the angular velocity of the DC motor. From (8), one can easily obtain F_c as

$$F_c = \frac{K_m}{R r_p} V_{DC} - \frac{K_m K_E}{R r_p^2} x_2. \tag{9}$$

3 Control Design and Stability Analysis

3.1 Controller Design

The control objective is to design a controller that drives the states of the system, $\mathbf{X} \in \Re^6$, to their respective desired trajectories, $\mathbf{X}^d \in \Re^6$, in the presence of the perturbations (4) and (5), and friction (7). The controller is required to maintain robust stability and robust performance despite the perturbations.

In conventional SMC, the system's motion under sliding mode has a dimension less than the state space. In the ISMC developed by Utkin and Shi [59], the integral term breaks out of this point and increases sliding mode dimension to equal that of the state space and system trajectory emanates from the sliding manifold. Hence, the reaching phase is eliminated, and robustness against matched uncertainties is guaranteed throughout the state space.

When (6) applies, the perturbed crane model (3) can be rewritten in compact form given by:

$$\dot{\mathbf{X}} = \mathbf{AX} + \mathbf{B} \left(F_c' + \delta \right) + \mathbf{G} + \Delta; \tag{10}$$

where $\mathbf{X} \in \Re^6$ is the state vector, F_c' is the perturbed control input, $\delta \in \Re^6$ is the vector of matched uncertainties, and $\Delta \in \Re^6$ is the vector of unmatched uncertainties. When we, for simplicity, drop the state and time dependency notations, the vectors δ and Δ, and the matrices $\mathbf{A} \in \Re^{6 \times 6}$, $\mathbf{B} \in \Re^6$ and $\mathbf{G} \in \Re^6$ are here defined as:

$$\mathbf{A} = \begin{bmatrix} 0 & 1 & 0 & 0 & 0 & 0 \\ 0 & 0 & 0 & 0 & 0 & 0 \\ 0 & 0 & 0 & 1 & 0 & 0 \\ 0 & 0 & 0 & 0 & 0 & 0 \\ 0 & 0 & 0 & 0 & 0 & 1 \\ 0 & 0 & 0 & 0 & 0 & 0 \end{bmatrix}; \quad \mathbf{B} = \begin{bmatrix} 0 \\ b_1 \\ 0 \\ b_2 \\ 0 \\ b_3 \end{bmatrix}; \quad \mathbf{G} = \begin{bmatrix} 0 \\ g_1 \\ 0 \\ g_2 \\ 0 \\ g_3 \end{bmatrix};$$

$$\delta = \begin{bmatrix} 0 \\ \delta g_1 + \delta \tilde{b}_1 F_c \\ 0 \\ \delta \tilde{g}_2 + \delta \tilde{b}_2 F_c \\ 0 \\ \delta \tilde{g}_3 + \delta \tilde{b}_3 F_c \end{bmatrix}; \quad \Delta = \begin{bmatrix} 0 \\ \Delta g_1 + \Delta b_1 \\ 0 \\ \Delta g_2 + \Delta b_2 \\ 0 \\ \Delta g_3 + \Delta b_3 \end{bmatrix}.$$

Define the state tracking error as $\mathbf{e}(t) = \mathbf{X} - \mathbf{X}^d$, where $\mathbf{e}(t) \in \Re^6$ is the error between the actual states trajectories ($\mathbf{X} \in \Re^6$), and the desired states trajectories ($\mathbf{X}^d \in \Re^6$). Design the integral ISMC surface as:

$$\xi(\mathbf{e}, t) = \Gamma \left[\mathbf{e}(t) - \mathbf{e}(0) \right] - \int_0^t \Gamma (\mathbf{A} - \mathbf{BF}) \mathbf{e}(\tau) d\tau; \tag{11}$$

where $\Gamma \in \Re^6$, and $\mathbf{F} \in \Re^6$ are design parameters that characterize the sliding surface.

Assumption 3 The input distribution matrix, $\mathbf{B}$, has full rank $\forall \mathbf{X} \in \Re^6$.

Remark 2 The vector $\mathbf{\Gamma}$ is designed to ensure that the product $\mathbf{\Gamma B}$ is non-singular. It is easy to achieved this since matrix $\mathbf{B}$ has full rank and $\mathbf{\Gamma}$ is a free parameter. On the other hand, $\mathbf{F}$ is designed using pole placement technique such that $(\mathbf{A} - \mathbf{BF})$ is *Hurwitz*.

Due to its merits, we adopt the equivalent control (12), where u_{eq}, and u_{sw} (to be designed) are known as the equivalent control, and the switching control, respectively.

$$F_{\text{c}} = u_{\text{eq}} + u_{\text{sw}}. \tag{12}$$

Only u_{eq} is applied during the sliding phase to maintain the variables sliding along the manifold $\xi(\mathbf{e}, t) = 0$ and eventually converge to the origin. For the reaching phase, both u_{eq} and u_{sw} are applied. The time derivative of (11) is given by:

$$\dot{\xi}(\mathbf{e}, t) = \mathbf{\Gamma}\dot{\mathbf{X}} - \mathbf{\Gamma}(\mathbf{A} - \mathbf{BF})\mathbf{e}(t). \tag{13}$$

When (10) applies, and argument notation henceforth dropped, $\dot{\xi}(\mathbf{e}, t)$ can be expressed as:

$$\dot{\xi} = \mathbf{\Gamma}\left[\mathbf{AX} + \mathbf{B}\left(F_{\text{c}}' + \delta\right) + \mathbf{G} + \mathbf{\Delta}\right] - \mathbf{\Gamma AX} + \mathbf{\Gamma BFe}(t); \tag{14}$$

which by invoking (12), and simplifying; one obtains:

$$\dot{\xi} = \mathbf{\Gamma B}\left(u_{\text{eq}} + u_{\text{sw}}\right) + \mathbf{\Gamma B}\delta + \mathbf{\Gamma G} + \mathbf{\Gamma \Delta} + \mathbf{\Gamma BFe}(t). \tag{15}$$

One's objective is to have $\xi = \dot{\xi} = 0$ in finite time (i.e., sliding motion along $\xi = 0$). Hence, considering (15) and Assumption 1, u_{eq} is here designed as:

$$u_{\text{eq}} = -(\mathbf{\Gamma B})^{-1}\mathbf{\Gamma G} - \mathbf{Fe}(t). \tag{16}$$

Applying (16) to (15), one easily obtains $\dot{\xi}$ as:

$$\dot{\xi} = \mathbf{\Gamma B}u_{\text{sw}} + \mathbf{\Gamma B}\delta + \mathbf{\Gamma \Delta}. \tag{17}$$

Remark 3 In conventional SMC, the law u_{sw} makes the control effort to suffer from high-frequency switching (i.e., the chattering issue). Chattering makes control effort difficult to track by most practical actuators. One solution is boundary layer control. However, the boundary method may result in the degradation of tracking and robustness. Chattering can be significantly attenuated using STC (a second-order SMC) that ensures a continuous control effort.

3.1.1 The STC and MSTC Algorithms

The second-order STC algorithm has been defined as [37]:

$$\begin{cases} u_{\text{STC}} = -\lambda_1 |\xi|^{1/2} \, \text{sgn}(\xi) + w; \\ \dot{w} = -\lambda_3 \, \text{sgn}(\xi), \end{cases} \tag{18}$$

where λ_1, and λ_3 are the controller design parameters. The signum function $\text{sgn}(\cdot)$ is defined as:

$$\text{sgn}(\xi) := \begin{cases} -1, & \text{if } \xi < 0; \\ 0, & \text{if } \xi = 0; \\ 1, & \text{if } \xi > 0. \end{cases} \tag{19}$$

The controller gains λ_1 and λ_3 in (18) are usually required to be high in order to accelerate the convergence of the sling variable $\xi(\mathbf{e}, t)$ to the origin. However, for chattering to have low amplitudes, it is required that these gains have small values. To circumvent this problem, researchers such as [55] and [56] proposed the following modified algorithm, here referred to as the MSTC:

$$\begin{cases} u_{\text{MSTC}} = -\lambda_1 |\xi|^{1/2} \, \text{sgn}(\xi) - \lambda_2 \xi + w; \\ \dot{w} = -\lambda_3 \, \text{sgn}(\xi) - \lambda_4 \xi, \end{cases} \tag{20}$$

where λ_1, λ_2, λ_3, and λ_4 are the controller parameters, with λ_1, and λ_3 as in (18).

3.1.2 The Proposed NSSTC Algorithm and Its Application

Using (20), one can achieve faster convergence of ξ to the origin. However, when the auxiliary variable $\dot{w}$ increases and consequently w increases, a longer settling time and larger overshoot of ξ is produced. These result in higher control effort amplitude. To address this issue, we propose the following novel NSSTC algorithm:

$$\begin{cases} u_{\text{NSSTC}} = -\lambda_1 |\xi|^y \, \text{sgn}(\xi) - \lambda_2 \xi \, \text{e}^{-\gamma t} + w; \\ \dot{w} = -\lambda_3 |\xi|^M \, \text{sgn}(\xi) - \lambda_4 \xi; \\ y = \frac{\theta - 1}{\theta}, M = \frac{\theta - 2}{\theta}. \end{cases} \tag{21}$$

The parameter $\theta \geq 2$ in (21) is referred to as the '*smoothness factor*,' while λ_1, λ_2, λ_3 and λ_4 are the controller parameters, with λ_1 and λ_3 as in (18) and (20), and γ is a small positive constant used to penalize the sliding surface overshoot and settling time. We will show that the control structure in (21) does not suffer, severely, the problems of (20) and relatively has some improved performance.

In summary, the objective here is to improve the classical STC algorithm (18) so as to improve the convergence speed of the sliding variable ξ while avoiding the earlier highlighted problems of (20).

Remark 4 The 'smoothness factor,' θ can be exploited to improve the control effort's smoothness. Also, the design parameter γ can be used to penalize the sliding surface and the control force peaks. Intelligent turning algorithms like neural networks or fuzzy logic may be employed to obtain these parameters' optimal values online.

Considering (17) and the proposed NSSTC algorithm (21), we design the switching control law, u_{sw}, as:

$$u_{sw} = -(\mathbf{\Gamma B})^{-1}\left[\lambda_1|\xi|^y \operatorname{sgn}(\xi) + \lambda_2\xi\, e^{-\gamma t}\right.$$
$$\left. + \int_0^t \left(\lambda_3|\xi|^M \operatorname{sgn}(\xi) + \lambda_4\xi\right)d\tau\right]. \tag{22}$$

And by submitting the foregoing into (17), one gets $\dot{\xi}$ as:

$$\dot{\xi}(\mathbf{e}, t) = -\lambda_1|\xi|^y \operatorname{sgn}(\xi) - \lambda_2\xi\, e^{-\gamma t}$$
$$- \int_0^t \left(\lambda_3|\xi|^M \operatorname{sgn}(\xi) + \lambda_4\xi\right)d\tau + \mathbf{\Gamma B\delta} + \mathbf{\Gamma\Delta}. \tag{23}$$

Set the uncertainty in (23) to be represented by $(\mathbf{\Gamma B\delta} + \mathbf{\Gamma\Delta}) = \phi$. In this connection, the ξ-dynamics (23) can be represented by the following closed-loop system.

$$\begin{cases} \dot{z}_1 = -\lambda_1|z_1|^y \operatorname{sgn}(z_1) - \lambda_2 z_1\, e^{-\gamma t} + z_2 + \phi; \\ \dot{z}_2 = -\lambda_3|z_1|^M \operatorname{sgn}(z_1) - \lambda_4 z_1, \end{cases} \tag{24}$$

where $[\xi \quad w]^T \triangleq [z_1 \quad z_2]^T = z$.

To simplify the subsequent analysis, we let

$$|\phi| \leq \varrho_1 + \varrho_2\|h\|, \tag{25}$$

where $\varrho_1 \in \Re^+$, $\varrho_2 \in \Re^+$, $\varrho_1 \neq 0$, and h as in (29), where ϱ_2 is sufficiently small.

Remark 5 It may have been noticed that the lumped uncertainty, ϕ, in (24) does not vanish at the origin since $\varrho_1 \neq 0$ in (25). As a result, the trajectories will not converge to the origin but will be ultimately bounded [60].

To this length, the control objective has been narrowed to steering to zero the sliding variable ξ and its time derivative $\dot{\xi}$ (or equivalently, dynamics (24)) in finite time with perturbations satisfying (24). Hence, the design of the NSSTC controller is formulated in the following theorem.

Theorem 1 *Consider system (24) with perturbation term satisfying (25) and controller parameters λ_1, λ_2, λ_3, λ_4, γ, and y designed in a way that matrix $\mathbf{A}_L$ is Hurwitz, then the trajectories of the system are globally ultimately bounded by:*

$$b = \sqrt{\frac{\lambda_{\max}(\mathbf{P})}{\lambda_{\min}(\mathbf{P})}} \frac{2\varrho_1\varepsilon}{(1-\tau)\left[\lambda_{\min}(\mathbf{Q}) - 2\varrho_2\varepsilon\right]}, \tag{26}$$

for $\varrho_1 \in \Re^+$, $\varrho_2 \leq \lambda_{\min}(\mathbf{Q})/2\varepsilon$ with a positive definite (PD) symmetric matrix $\mathbf{P}$, and $\tau \in (0, 1)$. Also, the trajectories will enter the manifold $\sigma_\omega = \left\{z \in \Re^2 \mid V(t, z) \leq \lambda_{\max}(\mathbf{P})\omega^2\right\}$ containing the origin in a time less than T_r, given by:

$$T_r = \theta\frac{\lambda_{\max}^y(\mathbf{P})}{\tau(\lambda_{\min}(\mathbf{Q}) - 2\varrho_2\varepsilon)}\left(V_0^{\frac{1}{\theta}} - \lambda_{\max}^{\frac{1}{\theta}}(\mathbf{P})\omega^{\frac{2}{\theta}}\right), \tag{27}$$

where

$$\omega \triangleq \frac{2\varrho_1\varepsilon}{(1-\tau)(\lambda_{\min}(\mathbf{Q}) - 2\varrho_2\varepsilon)}.$$

The proof of Theorem 1 is presented in Sect. 3.2.

3.2 Stability Analysis

At this juncture, the proof for Theorem 1 is presented. Like in Moreno's work [55], we examine a PD and radially unbounded Lyapunov function candidate given by:

$$V(t, z) = h^T \mathbf{P} h. \tag{28}$$

For the system to be globally stable, $\dot{V}(t, z)$ needs to be ND [61]. In (28), $h \in \Re^2$ is a new state vector introduced representing system (24), which is defined as:

$$h = [h_1 \quad h_2]^T = \left[|z_1|^y \operatorname{sign}(z_1) \quad z_2\right]^T, \tag{29}$$

while $\mathbf{P} \in \Re^{2\times 2}$ is a PD symmetric matrix, and is the solution to the algebraic Lyapunov equation given by:

$$\mathbf{A}_L^T\mathbf{P} + \mathbf{P}\mathbf{A}_L = -\mathbf{Q}. \tag{30}$$

Since the matrix $\mathbf{A}_L$ is Hurwitz, a PD matrix $\mathbf{Q}$ exists such that the foregoing is satisfied.

The time derivative of (29) is given by:

$$\dot{h} = \left[\frac{\partial}{\partial t}|z_1|^y \operatorname{sign}(z_1) \quad \frac{\partial}{\partial t}z_2\right]^T = \left[y|z_1|^{y-1}\dot{z}_1 \quad \dot{z}_2\right]^T$$

$$= \begin{bmatrix} y|z_1|^{y-1}\left(-\lambda_1|z_1|^y \operatorname{sgn}(z_1) - \lambda_2 z_1\, e^{-\gamma t} + z_2 + \phi\right) \\ -\lambda_3|z_1|^M \operatorname{sgn}(z_1) - \lambda_4 z_1 \end{bmatrix}$$

$$= \frac{1}{|z_1|^{\frac{1}{\theta}}}\begin{bmatrix} y\left(-\lambda_1|z_1|^y \operatorname{sgn}(z_1) - \lambda_2 z_1\, e^{-\gamma t} + z_2 + \phi\right) \\ -\lambda_3|z_1|^y \operatorname{sgn}(z_1) - \lambda_4|z_1|^{1/\theta} z_1 \end{bmatrix}$$

$$= \frac{1}{|z_1|^{\frac{1}{\theta}}}\left\{\begin{bmatrix} -y(\lambda_1 + \lambda_2\frac{|z_1|^{\frac{1}{\theta}}}{e^{\gamma t}})\, y & y \\ -\lambda_3 - \lambda_4|z_1|^{\frac{2}{\theta}} & 0 \end{bmatrix}\begin{bmatrix} h_1 \\ h_2 \end{bmatrix} + \begin{bmatrix} y\phi \\ 0 \end{bmatrix}\right\}$$

$$= |z_1|^{-\frac{1}{\theta}}(\mathbf{A}_L h + \Phi), \tag{31}$$

where $\Phi = \begin{bmatrix} y\phi & 0 \end{bmatrix}^T$. Hence, the transpose of (31) can be expressed as:

$$\dot{h}^T = |z_1|^{-\frac{1}{\theta}}\left(h^T\mathbf{A}_L^T + \Phi^T\right). \tag{32}$$

The total time derivative of (28) is given by:

$$\dot{V}(t, z) = \dot{h}^{\mathrm{T}} \mathbf{P} h + h^{\mathrm{T}} \mathbf{P} \dot{h}. \tag{33}$$

Invoking (31) and (32), the foregoing can be expressed as:

$$\dot{V}(t, z) = |z_1|^{-\frac{1}{\theta}} \left[h^{\mathrm{T}} \mathbf{A}_{\mathrm{L}}^{\mathrm{T}} \mathbf{P} h + \mathrm{h}^{\mathrm{T}} \mathbf{P} \mathbf{A}_{\mathrm{L}} h + 2 \Phi^{\mathrm{T}} \mathbf{P} h \right], \tag{34}$$

where the fact that $\Phi^{\mathrm{T}} \mathbf{P} h = \mathrm{h}^{\mathrm{T}} \mathbf{P} \Phi$ has been applied. The term $\Phi^{\mathrm{T}} \mathbf{P} h$ can further be simplified as follows:

$$\Phi^{\mathrm{T}} \mathbf{P} h = \begin{bmatrix} \mathrm{y}\phi & 0 \end{bmatrix} \begin{bmatrix} P_{11} & P_{12} \\ P_{12} & P_{22} \end{bmatrix} \begin{bmatrix} |z_1|^{\mathrm{y}} \operatorname{sign}(z_1) \\ z_2 \end{bmatrix}$$

$$= \mathrm{y}\phi \mathrm{h}^{\mathrm{T}} \begin{bmatrix} P_{11} \\ P_{12} \end{bmatrix}. \tag{35}$$

Hence, considering (30) and (35) one can represent (34) as:

$$\dot{V}(t, z) = -|z_1|^{-\frac{1}{\theta}} \left[h^{\mathrm{T}} \mathbf{Q} h - 2 \phi h^{\mathrm{T}} \varepsilon \right], \tag{36}$$

where $\varepsilon = [\mathrm{y} P_{11} \quad \mathrm{y} P_{12}]^{\mathrm{T}}$.

One can easily show that the candidate Lyapunov function (28) can be both sides bounded as follows:

$$\lambda_{\min}(\mathbf{P}) \|\mathrm{h}\|^2 \le V(t, z) \le \lambda_{\max}(\mathbf{P}) \|\mathrm{h}\|^2, \tag{37}$$

where $\lambda_{\min}$ and $\lambda_{\max}$ are, respectively, the smallest and the largest eigenvalues of the matrix $\mathbf{P}$ and $\|h\|$ is the *Frobenius norm* of h. From (37), the below inequalities also hold.

$$\begin{cases} \|h\|^2 \ge \dfrac{V(t, z)}{\lambda_{\max}(\mathbf{P})}; \\ \|h\|^2 \le \dfrac{V(t, z)}{\lambda_{\min}(\mathbf{P})}. \end{cases} \tag{38}$$

Similarly, it can easily be shown that the following inequality set holds for $\dot{V}(t, z)$.

$$\begin{cases} -\dfrac{1}{|z_1|^{\frac{1}{\theta}}} \lambda_{\max}(\mathbf{Q}) \|h\|^2 \le \dot{V}(t, z) \le -\dfrac{1}{|z_1|^{\frac{1}{\theta}}} \lambda_{\min}(\mathbf{Q}) \|h\|^2; \\ \|h\|^2 \ge \dfrac{-\dot{V}(t, z)}{|z_1|^{-\frac{1}{\theta}} \lambda_{\max}(\mathbf{Q})}; \\ \|h\|^2 \le \dfrac{-\dot{V}(t, z)}{|z_1|^{-\frac{1}{\theta}} \lambda_{\min}(\mathbf{Q})}. \end{cases} \tag{39}$$

Along (25), it is easy to show that (36) is given by:

$$\dot{V}(t, z) \le -|z_1|^{-\frac{1}{\theta}} \left[h^{\mathrm{T}} \mathbf{Q} h - 2 (\varrho_1 + \varrho_2 \|h\|) \|h\| \varepsilon \right], \tag{40}$$

which along inequality (39) and using the fact that $|z_1|^{\frac{1}{\theta}} \le \|h\|$ and $\mathbf{Q}$ is PD and symmetric, can be expressed as:
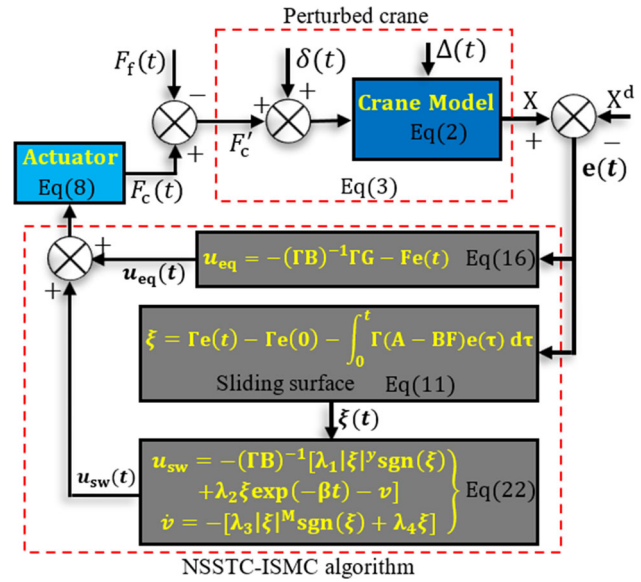

Fig. 3 Control system configuration

$$\dot{V}(t, z) \le -|z_1|^{-\frac{1}{\theta}} \left[\lambda_{\min}(\mathbf{Q}) \|h\| - 2 (\varrho_1 + \varrho_2 \|h\|) \|h\| \varepsilon \right]$$

$$\le -|z_1|^{-\frac{1}{\theta}} \|h\| \left[(\lambda_{\min}(\mathbf{Q}) - 2\varrho_2 \varepsilon) \|h\| - 2\varrho_1 \varepsilon \right]. \tag{41}$$

If we set $\|h\| = \tau \|h\| + (1 - \tau) \|h\|$ (which is true $\forall \tau \in (0, 1)$), then for small enough ϱ_2 such that the following holds:

$$\varrho_2 \le \frac{\lambda_{\min}(Q)}{2\varepsilon}; \tag{42}$$

then for every $\varrho_1 > 0$, and $\tau \in (0, 1)$, it can be obtained, from (41), that

$$\dot{V}(t, z) \le -\sqrt{\frac{V^{\mathrm{M}}(\cdot)}{\lambda_{\max}^{\mathrm{M}}(\mathbf{P})}} \left[\beta \tau \|h\| + \beta (1 - \tau) \|h\| - 2\varrho_1 \varepsilon \right], \tag{43}$$

where $\beta = (\lambda_{\min}(\mathbf{Q}) - 2\varrho_2 \varepsilon)$.

Remark 6 In the preceding equation, whether or not $\dot{V}(t, z)$ is negative definite (ND) depends on whether or not the following two conditions are satisfied:

C1. $\lambda_{\min}(\mathbf{Q}) \ge 2\varrho_2 \varepsilon$;
C2. $\beta (1 - \tau) \|h\| \ge 2\varrho_1 \varepsilon$.

Along (38), condition **C2** can be equivalently expressed as:

$$\|h\| \ge \frac{2\varrho_1 \varepsilon}{\beta (1 - \tau)} \ge \sqrt{\frac{V(\cdot)}{\lambda_{\max}(\mathbf{P})}} = \omega, \tag{44}$$

Table 2 Simulation model parameters

Parameters			
$m_c = 50\,\text{kg}$	$m_h = 12\,\text{kg}$	$m_p = 4.5\,\text{kg}$	$L_1 = 3\,\text{m}$
$L_2 = 0.3\,\text{m}$	$g = 9.8\,\text{m/s}^2$	$\alpha_1 = 3.9$	$\alpha_2 = 2.2$
$K_m = 0.24\,\text{Nm/A}$	$\beta_1 = 50$	$\beta_2 = 0.9$	$\beta_3 = 70$
$K_E = 0.24\,\text{V/rad/s}$	$r_p = 0.07\,\text{m/s}$	$\alpha_3 = 0.15$	$R = 3.35\,\Omega$

where ω denotes the boundary of the manifold σ. Hence, one gets the systems stable manifold as $V(\cdot) \leq \lambda_{\max}(\mathbf{P})\omega^2$, describing the interior of the manifold. When condition (44) applies, along the boundary of σ, (43) reduces to:

$$
\begin{aligned}
\dot{V}(t, z) &\leq -\sqrt{\frac{V^{\mathrm{M}}(\cdot)}{\lambda_{\max}^{\mathrm{M}}(\mathbf{P})}} \beta\tau \sqrt{\frac{V(\cdot)}{\lambda_{\max}(\mathbf{P})}}, \forall \|h\| \geq \omega \\
&\leq -\tau \left(\lambda_{\min}(\mathbf{Q}) - 2\varrho_2\varepsilon\right) \frac{V^{\mathrm{y}}(t, h)}{\lambda_{\max}^{\mathrm{y}}(\mathbf{P})}, \forall \|h\| \geq \omega.
\end{aligned}
\tag{45}
$$

Ultimately, any trajectory starting from initial state z_0 will converge to the set $\sigma = z \in \Re^2 | V(t, z) \leq \lambda_{\max}\omega^2$ in finite time, T_r, which by using Bihari's inequality [60] and the separation principle can be computed as:

$$
T_r = \theta \frac{\lambda_{\max}^{\mathrm{y}}(\mathbf{P})}{\tau \left(\lambda_{\min}(\mathbf{Q}) - 2\varrho_2\varepsilon\right)} \left(V_0^{\frac{1}{\theta}} - \lambda_{\max}^{\frac{1}{\theta}}(\mathbf{P})\omega^{\frac{2}{\theta}}\right),
\tag{46}
$$

and remain in σ such that $\|z\| \leq \omega$ for all future times $t \geq t_0 + T_r$ with b as in (26).

Remark 7 Since $\varrho_1 \neq 0$, trajectories will not converge to the origin, but may converge to the set σ which may contain the origin, and will be globally ultimately bounded. This means that $\exists b > 0$ and for every $a > 0$, $\exists T = T(a, b) \geq 0 | \|z(t_0)\| \leq a \rightarrow \|z\| \leq b$, $\forall t \geq t_0 + T_r$.

The following assumption is considered for the purpose of the control applications in Sect. 4.

Assumption 4 For the purpose of simulation, the matched uncertainties due to un-modelled dynamics, parametric variations, and external disturbance that enter the system through the same channel as the control force, F_c, are taken as $\delta\tilde{g}_i(\mathbf{X}) + \delta\tilde{b}_i(\mathbf{X}) = 2\sin 3t + \cos t + 2$. Additionally, the unmatched uncertainties are taken as $\Delta g_i(\mathbf{X}) + \Delta b_i(\mathbf{X})$, $(i = 1, 2, 3)$, representing some random fluctuations in the range $[-0.1\ 0.1]$.

Figure 3 shows the configuration of the overall system with the proposed NSSTC-ISMC strategy. The error vector, $\mathbf{e}(t) \in \Re^6$, is obtained as the discrepancy between the actual states, $\mathbf{X}(t) \in \Re^6$, and their corresponding set points, $\mathbf{X}^d(t) \in \Re^6$. This error vector is taken as an input by the equivalent control and sliding variable blocks. As it can also be seen,

Table 3 Control design parameters

Strategy	Design parameters
MSTC-ISMC	$\mathbf{F} = \begin{bmatrix} 105 & 190 & -2000 & -815 & 55 & 60 \end{bmatrix}$
	$\mathbf{\Gamma} = \begin{bmatrix} 950 & 480 & 2150 & 2250 & -1950 & -1200 \end{bmatrix}$
	$\lambda_1 = 30 \quad \lambda_2 = 30 \quad \lambda_3 = 20 \quad \lambda_4 = 5$
NSSTC-ISMC	$\mathbf{F} = \begin{bmatrix} 105 & 190 & -2000 & -815 & 55 & 60 \end{bmatrix}$
	$\mathbf{\Gamma} = \begin{bmatrix} 950 & 480 & 2150 & 2250 & -1950 & -1200 \end{bmatrix}$
	$\lambda_1 = \lambda_2 = 30 \quad \lambda_3 = 20 \quad \lambda_4 = 5 \quad \gamma = -50$

the sliding variable $\xi(t)$ is taken as an input by the switching control block to generate the $u_{\mathrm{sw}}(t)$. As the sum of $u_{\mathrm{sw}}(t)$ and $u_{\mathrm{eq}}(t)$, the input to the trolley actuator is then obtained. The actuator physical force $F_c(t)$ minus the frictional force $F_f(t)$ is used to drive the perturbed system (3).

4 Results and Discussion

Below this section, the effectiveness of the proposed NSSTC-ISMC algorithm will be demonstrated. The NSSTC-ISMC is compared with those obtained using the existing MSTC algorithm in the literature. For fair comparative analysis, the ISMC method is used to design the sliding surface for the existing MSTC algorithm (forming a hybrid MSTC-ISMC control scheme). Simulations experiments were conducted within the MATLAB software using the Runge–Kutta numerical solver with an iteration step size of 0.001. It is to be noted that Assumption 4 applies. Crane and control parameters are accepted as in Tables 2 and 3, respectively.

The performances of the NSSTC-ISMC is also compared against those of MSTC-ISMC and the classical ISMC algorithms. The ISMC is designed based on the exponential reaching law given by:

$$
F_{c(\mathrm{ISMC})} = u_{\mathrm{eq}} - \mathbf{\Gamma B}[\mathrm{k}\xi(\mathbf{e}, t) + \eta\, \mathrm{sgn}\{\xi(\mathbf{e}, t)\}],
\tag{47}
$$

where $\mathrm{k}\xi(\mathbf{e}, t)$ is the exponential term and $\mathrm{k}, \eta > 0$. For the purpose of comparison, u_{eq} in (47) is the same as in (16).

Figure 4 shows the responses obtained when the proposed NSSTC-ISMC control strategy's efficacy is compared against those of the MSTC-ISMC and the conventional ISMC methods. Zero initial conditions for the crane states were

Fig. 4 Tracking responses, **a** cart position, **b** cart velocity, **c** hook sway, **d** hook sway velocity, **e** load sway, **f** load sway velocity
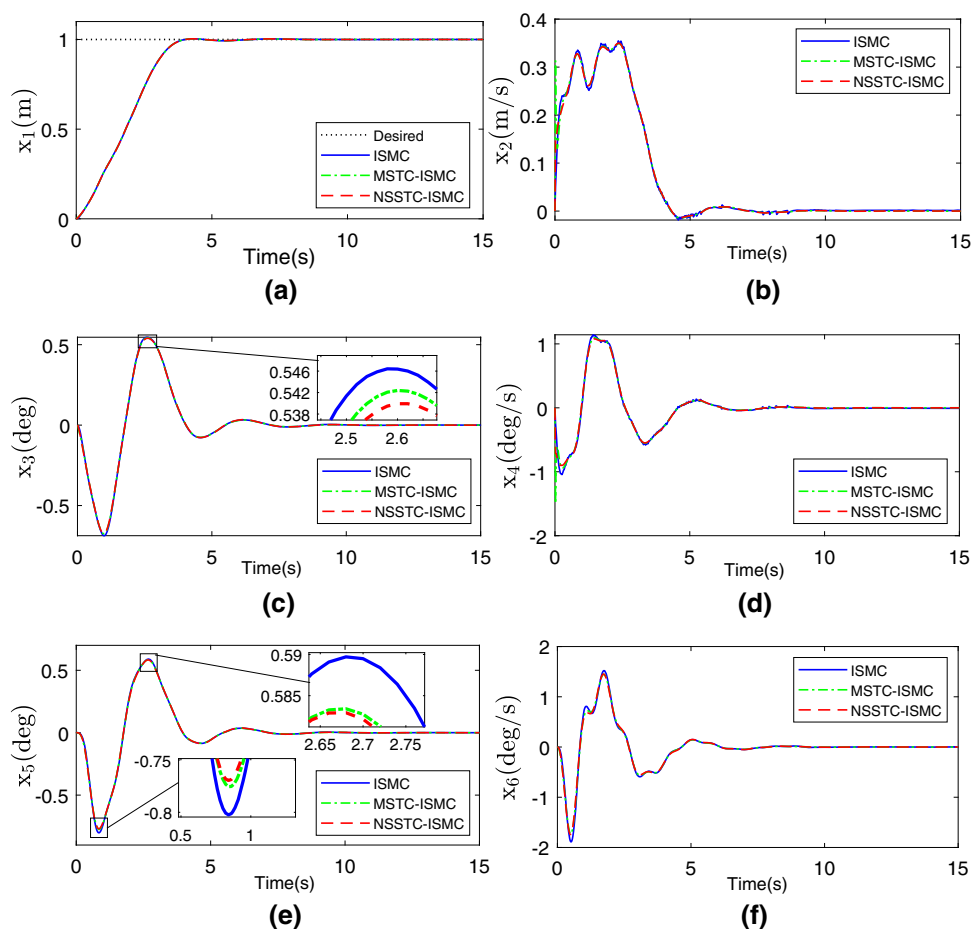
assumed. Moreover, for comparison, the same model parameters and sliding manifold parameters are used.

One can see from the responses that the cart tracked the desired 1 m position in about 4 s, and the controllers effectively suppress both hook and payload sways. Additionally, as respectively shown in Fig. 4c and e, the performance of the proposed NSSTC-ISMC is slightly more effective with regards to hook sway and payload sway suppression as compared to the other two controllers.

In Fig. 5a and b, the control efforts and the sliding surfaces for the three controllers are compared, respectively. It may have been noted that the control effort for the conventional ISMC chatters, while no chattering was observed for the case using the MSTC-ISMC. However, a much greater control effort is required, and the sliding variable overshoots. Similar to the MSTC-ISMC, the proposed NSSTC-ISMC has no chattering. However, a relatively much lower control effort is required, and the sliding variable overshoot is suppressed. The profiles for the matched and unmatched uncertainties are depicted in Fig. 5c and d, respectively. It is to be noted that, until otherwise expressed, below this section, all horizontal axes represent time in seconds.

To further investigate the claims of improvements in the control effort and the sliding variable achieved using the proposed NSSTC-ISMC algorithm, like in the works of [32–36,62] we employ the MAE and the MSE criteria computed using (48) and (49), respectively.

$$\text{MAE} = \frac{\sum_{i=1}^{N} |S(\tau)|}{N}; \tag{48}$$

$$\text{MSE} = \frac{\sum_{i=1}^{N} S(\tau)^2}{N}, \tag{49}$$

where $S(\tau)$ is signal sampled at the τth instance, while N represents total samples count. The MAE and MSE values for the control application in Figs. 4 and 5 are depicted in Fig. 6. One can argue that the MAE and MSE analysis results further support the claims in the preceding paragraph.

Zero initial conditions were taken for the previous control application. Nevertheless, in real cranes, this is not always the scenario. Control application was repeated to test the effectiveness of the three control strategies for nonzero initial conditions given by $\mathbf{X}_0 = \begin{bmatrix} 1.5 & 0.4 & 0.1 & 0 & 0.1 & 0.1 \end{bmatrix}^T$, i.e., the driving cart was assumed to be at an initial position of 1.5 m from the datum point. The payload and the hook angles were

Fig. 5 Zero initial conditions tracking responses, **a** control effort, **b** sliding variable, **c** matched uncertainty, **d** unmatched uncertainty
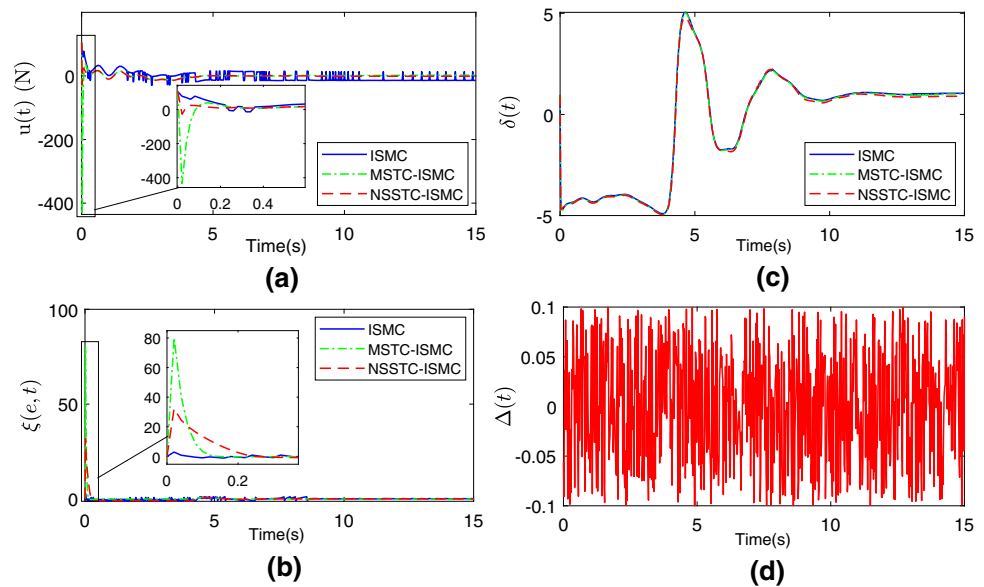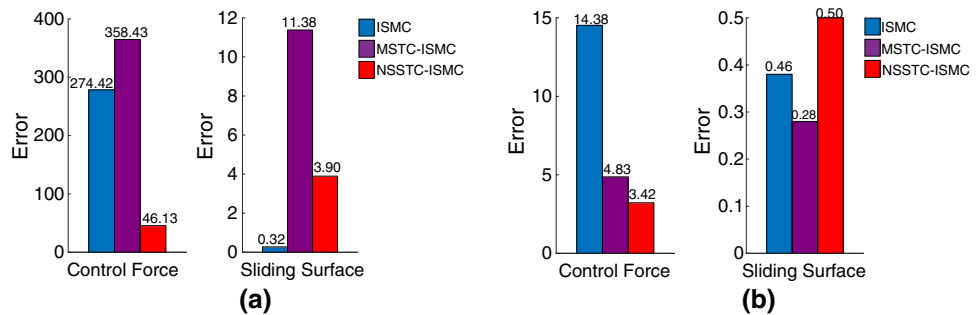

Fig. 6 Error analysis for the ISMC, MSTC-ISMC and NSSTC-ISMC controllers from zero initial states, **a** MSE, **b** MAE

at an angle of about 6^0 from the vertical reference of 0^0 when the command to track a 1 m position was applied. Figure 7 shows the evolution of the state trajectories from nonzero initial conditions. From the figure, one can see that the cart tracked the desired 1 m position in about 7 s, and the controllers effectively suppress both hook and payload sways. Like in the previous control application, the performance of the proposed NSSTC-ISMC is slightly more effective when compared to the other two controllers. It is worth pointing out that the driving cart reached the desired position in about 7 s, slower than the case where zero initial conditions are assumed (see Fig. 4). This is because, since the payload and hook sways are non-actuated state variables, the controllers used the driving cart's motion (i.e., the actuated state variable) to regulate or suppress the initial and residual sways indirectly. The reader may refer to the cart's velocity (Fig. 7b) to see how the cart's direction of travel changed while the driving cart tracked the desired trajectory, and at the same time, attenuated the pendulum-like motions of the payload and hook.

In Fig. 8a and b, the control efforts and the sliding surfaces for the three controllers are compared. It may have been noticed that the control effort for the conventional ISMC

chatters, while no chattering is observed for the case using the MSTC-ISMC, but a greater control effort is required, and the sliding variable overshoots. Similar to the MSTC-ISMC, the proposed NSSTC-ISMC has no chattering; however, a relatively lesser control effort is required, and the sliding variable overshoot is suppressed. The profiles for the matched and unmatched uncertainties are depicted in Fig. 8c and d, respectively.

Like in the previous control application, the MAE and MSE values for the control application in Figs. 7 and 8 (for nonzero initial conditions) are depicted in Fig. 9. Based on the MAE and MSE results, one can argue that the proposed NSSTC-ISMC algorithm's effectiveness is better compared to the two other controllers.

Remark 8 The chattering problem affects the fatigue life of actuators. Besides that, driving a system with such a high-frequency signal may excite the system's parasitic dynamics (which are of high frequencies). Nevertheless, one may employ boundary layer control to circumvent this problem when using conventional first-order SMC algorithms. However, studies have shown that using boundary layer control may reduce control resilience. This robustness reduction is attributed to the fact that the sliding variable is no longer con-

Fig. 7 Tracking responses for nonzero initial states, **a** cart position, **b** cart velocity, **c** hook sway, **d** hook velocity, **e** load sway, **f** load velocity
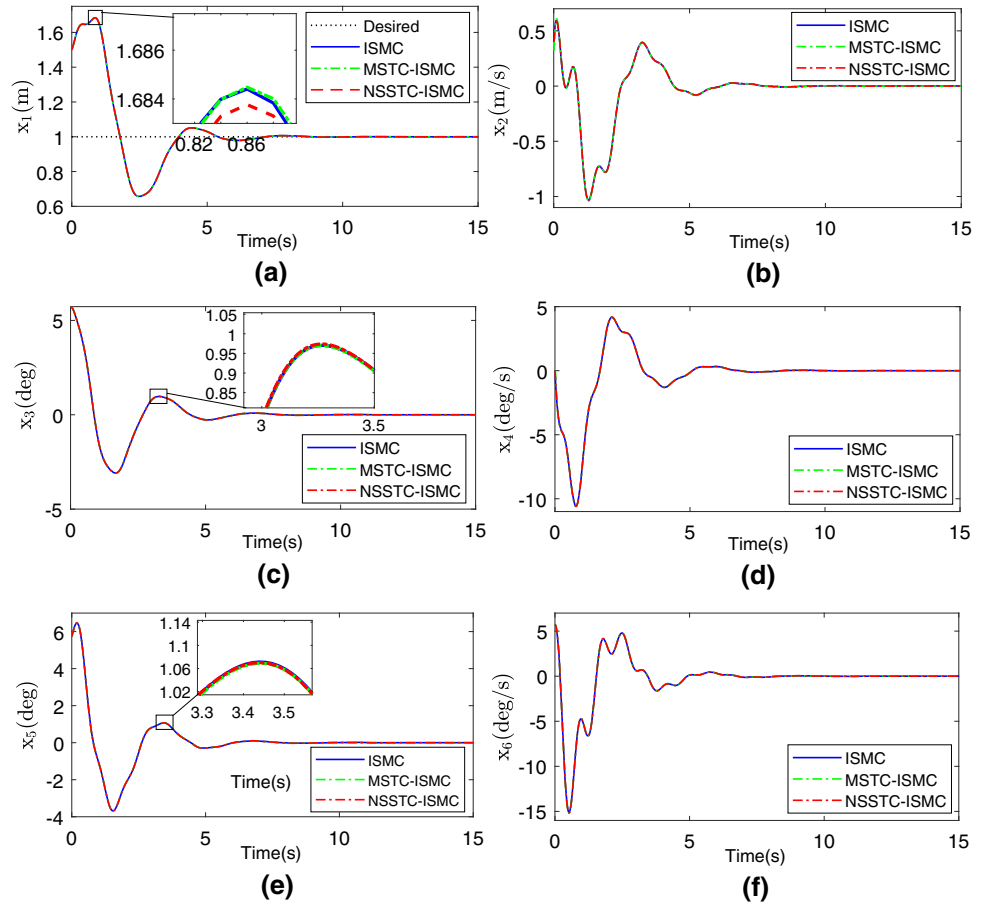

Fig. 8 Nonzero initial conditions tracking responses, **a** control effort, **b** sliding variable, **c** matched uncertainty, **d** unmatched uncertainty
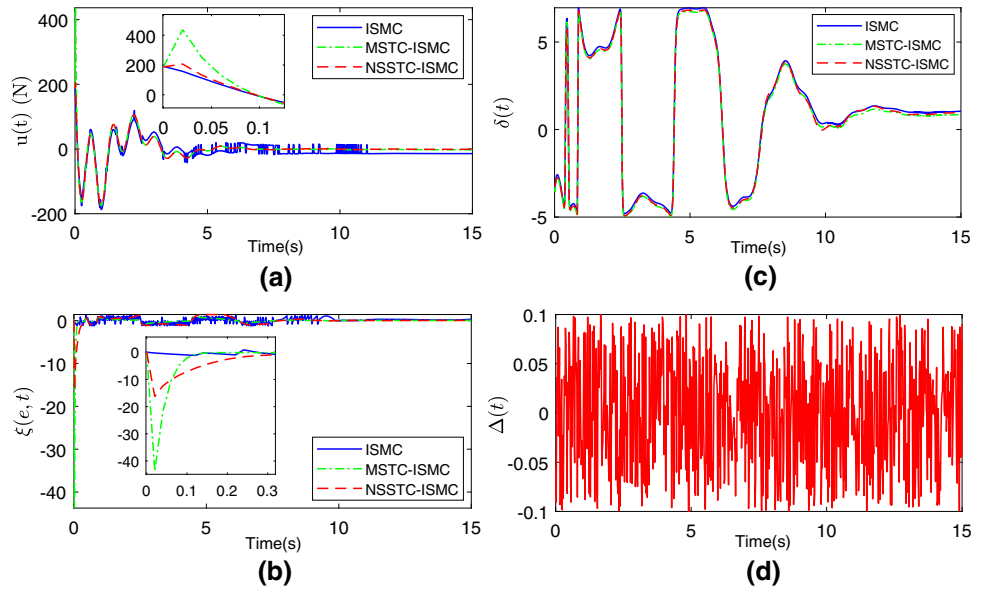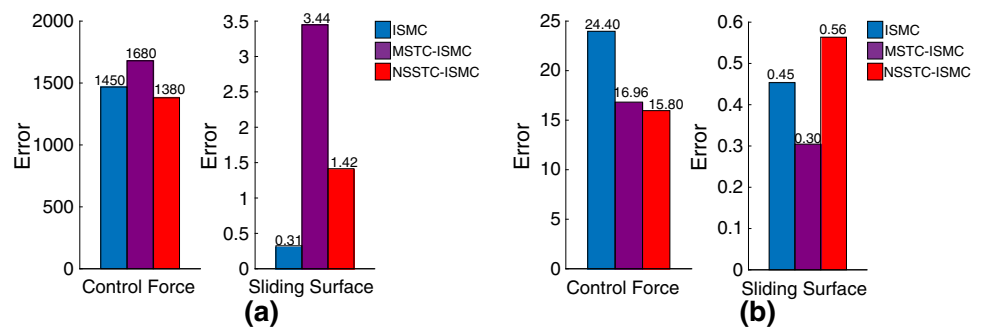
Fig. 9 Error analysis for ISMC, MSTC-ISMC, and NSSTC-ISMC controllers from nonzero initial states, **a** MSE, **b** MAE

fined to the sliding manifold but the neighbourhood around the manifold. Hence, control strategies (such as second-order STC) that attenuate chattering without compromising robustness are always preferred in practice.

5 Conclusions and Future Works

In overhead cranes, the presence of the double-pendulum effect, disturbances, and frictions make control more challenging. The paper devised a novel structure of a super-twisting algorithm that ensured the desired performance of a sixth-order nonlinear perturbed overhead crane. A hybrid control strategy formed by blending NSSTC and ISMC is proposed. The proposed method's efficacy has been investigated compared to those of a hybrid MSTC-ISMC and conventional ISMC control algorithms. The proposed NSSTC algorithm has been found to mitigate the sliding surface overshoot and alleviate the initial peak of the trolley control effort that can be encountered using the existing MSTC algorithm. By using a strict quadratic Lyapunov function, the closed-loop system has been shown to be finite-time stable.

In future work, the assumption that crane states are available for full-state feedback design may be addressed using a state observer. In this way, the efficacy of the proposed control method could be investigated on an industrial crane. Additionally, the '*smoothness factor*,' θ and the design parameter γ may be optimally obtained by exploiting intelligent turning algorithms like neural networks or fuzzy logic.

Compliance with Ethical Standards

Conflict of interest The authors declare that they have no conflict of interest.

References

1. Romero, J.G.; Donaire, A.; Ortega, R.; Borjad, P.: Global stabilisation of underactuated mechanical systems via PID passivity-based control. Automatica **96**, 178–185 (2018)
2. Shah, I.; Rehman, F.U.: Smooth higher-order sliding mode control of a class of underactuated mechanical systems. Arab. J. Sci. Eng. **42**, 5147–5164 (2017)
3. Baklouti, A.; Nguyen, N.; Mhenni, F.; Choley, J.; Mlika, A.: Dynamic fault tree generation for safety-critical systems within a systems engineering approach. IEEE Syst. J. **14**(1), 1512–1522 (2020)
4. Xueyan, X.; Jinkun, L.: PDE modelling and vibration control of overhead crane bridge with unknown control directions and parametric uncertainties. IET Control Theory Appl. **14**(1), 116–126 (2020)
5. Shengzeng, Z.; Xiongxiong, H.; Haiyue, Z.; Qianga, C.; Yuanjinga, F.: Partially saturated coupled-dissipation control for underactuated overhead cranes. Mech. Syst. Signal Process. **136**, 1–17 (2020)
6. Tuan, L.A.; Lee, S.G.: 3D cooperative control of tower cranes using robust adaptive techniques. J. Franklin Inst. **354**(18), 8333–8357 (2017)
7. La, V.D.; Nguyen, K.T.: Combination of input shaping and radial spring-damper to reduce tridirectional vibration of crane payload. Mech. Syst. Signal Process. **116**, 310–321 (2019)
8. Chen, H.; Fang, Y.; Sun, N.: Optimal trajectory planning and tracking control method for overhead cranes. IET Control Theory Appl. **10**(6), 692–699 (2016)
9. Wu, Z.; Xia, X.: Optimal motion planning for overhead cranes. IET Control Theory Appl. **8**(17), 1833–1842 (2014)
10. Arabasi, S.; Masoud, Z.: Simultaneous travel and hoist maneuver input shaping control using frequency modulation. Shock Vib. **2017**, 1–12 (2017)
11. Caporali, R.P.L.: Iterative method for controlling with a command profile the sway of a payload for gantry and overhead traveling cranes. Int. J. Innov. Comput. Inform. Control **14**(3), 1095–1112 (2018)
12. Chen, J., Huo, X., Li, C., Xu, F.: Sway elimination for hoisting rod based on input shaping method. In: Proceedings of 2017 Chinese Automation Congress, Jinan, October 20–22, pp. 4055–4060 (2017)
13. Alhazza, K.; Masoud, Z.; Alotaibi, N.: A smooth wave-form shaped command with flexible maneuvering time: analysis and experiments. Asian J. Control **18**(4), 1376–1384 (2016)
14. Bashir, N.M.; Bature, A.A.; Abdullahi, A.M.: Pole placement control of a 2D gantry crane system with varying pole locations. Appl. Model. Simul. **2**(3), 8–16 (2018)
15. Ramli, L.; Mohamed, Z.; Efe, M.O.; Lazim, I.M.; Jaafar, H.I.: Efficient swing control of an overhead crane with simultaneous payload hoisting and external disturbances. Mech. Syst. Signal Process. **135**, 1–17 (2020)

16. Cellmer, A.; Banach, B.; Piotrowski, R.: Design of modified PID controllers for 3D crane control. In: Proceedings of KKA 2017-The 19th Polish Control Conference, Kraków, June 18–21, pp 77–86 (2017)

17. Yuslinda, S.; Jaafar, H.I.; Hazriq, I.; Razif, N.R.: The effects of auto-tuned method in PID and PD control scheme for gantry crane system. Int. J. Soft Comput. Eng. **4**(6), 121–125 (2015)

18. Alhassan, A.; Danapalasingam, K.A.; Shehu, M.; Abdullahi, A.M.; Tijjani, A.S.: Closed-loop schemes for position and sway control of a gantry crane system. Int. J. Simul. Syst. Sci. Technol. **17**(32), 28.1–28.8 (2016)

19. Jolevski, D.; Bego, O.: Model predictive control of gantry/bridge crane with anti-sway algorithm. J. Mech. Sci. Technol. **29**(2), 827–834 (2015)

20. Benhellal, B.; Hamerlain, M.; Rahmani, Y.: Decoupled adaptive neuro-interval type-2 fuzzy sliding mode control applied in a 3Dcrane system. Arab. J. Sci. Eng. **43**, 2725–2733 (2018)

21. Shehu, M.A.; Li, A.; Huang, B.; Wang, Y.; Liu, B.: Comparative analysis of neural-network and fuzzy auto-tuning sliding mode controls for overhead cranes under payload and cable variations. J. Control Sci. Eng. **2019**, 1–13 (2019)

22. Ngo, Q.H.; Hong, K.S.: Adaptive sliding mode control of container cranes. IET Control Theory Appl. **6**(5), 662–668 (2012)

23. Lin, T.; Lin, Y.; Zirkohi, M.M.; Huang, H.: Direct adaptive fuzzy moving sliding mode proportional integral tracking control of a three-dimensional overhead crane. J. Dyn. Syst., Meas. Control **138**(10), 1–11 (2016)

24. Tuan, L.A.; Lee, S.G.: Modeling and advanced sliding mode controls of crawler cranes considering wire rope elasticity and complicated operations. Mech. Syst. Signal Process. **103**, 250–263 (2018)

25. Tuan, L.A.; Cuong, H.M.; Trieu, P.V.; Nho, L.C.; Thuan, V.D.; Anh, L.V.: Adaptive neural network sliding mode control of shipboard container cranes considering actuator backlash. Mech. Syst. Signal Process. **112**, 233–250 (2018)

26. Zhang, M.; Ma, X.; Song, R.; Rong, X.; Tian, G.; Tian, X.; Li, Y.: Adaptive proportional-derivative sliding mode control law with improved transient performance for underactuated overhead crane Systems. IEEE/CAA J. Autom. Sin. **5**(3), 683–690 (2018)

27. Yakut, O.: Application of intelligent sliding mode control with moving sliding surface for overhead cranes. Neural Comput. Appl. **24**(6), 1369–1379 (2014)

28. Ngo, Q.H.; Nguyen, N.P.: Sliding mode control design with the time varying parameters of the sliding surface of an offshore container crane. In: Proceedings of 2017 11th Asian Control Conference, Gold Coast, December 17–20, pp. 2669–2674 (2017)

29. Vázquez, C.; Fridman, L.; Collado, J.; Castillo, I.: Second-order sliding mode control of a perturbed-crane. J. Dyn. Syst. Meas. Control **137**(8), 1–7 (2015)

30. Weimin, X.; Xiang, Z.; Yuqiang, L.; Mengjie, Z.; Yuyang, L.: Adaptive dynamic sliding mode control for overhead cranes. In: Proceedings of the 2015 34th Chinese Control Conference, Hangzhou, July 28–30, pp. 3287–3292 (2015)

31. Defoort, M.; Maneeratanaporn, J.; Murakami, T.: Integral sliding mode antisway control of an underactuated overhead crane system. In: Proceedings of 2012 9th France–Japan and 7th Europe–Asia Congress on Mechatronics (MECATRONICS)/13th Int'l Workshop on Research and Education in Mechatronics (REM), Paris, November 21–23, 2012, pp. 71–77 (2012)

32. Martinez, D.I.; de Jesús Rubio, J.; Vargas, T.M.; Garcia, V.; Ochoa, G.; Balcazar, R.; Cruz, D.R.; Aguilar, A.; Novoa, J.F.; Aguilar-Ibañez, C.: Stabilization of robots with a regulator containing the sigmoid mapping. IEEE Access **8**, 89479–89488 (2020)

33. Rubio, J.D.J.; Ochoa, G.; Mujica-Vargas, D.; Garcia, E.; Balcazar, R.; Elias, I.; Cruz, D.R.; Juarez, C.F.; Aguilar, A.; Novoa, J.F.: Structure regulator for the perturbations attenuation in a quadrotor. IEEE Access **7**, 138244–138252 (2019)

34. Escobedo-Alva, J.O.; Garcí-a-Estrada, E.C.; Páramo-Carranza, L.A.; Meda-Campaña, J.A.; Tapia-Herrera, R.: Theoretical application of a hybrid observer on altitude tracking of quadrotor losing GPS signal. IEEE Access **6**, 76900–76908 (2018)

35. Rubio, J.D.J.; Martinez, D.; Gutierrez, G.; Vargas, T.; Ochoa, G.; Balcazar, R.; Pacheco, J.; Meda Campaña, J.; Mújica-Vargas, D.: The perturbations estimation in two gas plants. IEEE Access **8**, 83081–83091 (2020)

36. García-Sánchez, J.R.; Tavera-Mosqueda, S.; Silva-Ortigoza, R.; Hernández-Guzmán, V.M.; Sandoval-Guti´errez, J.; Marcelino-Aranda, M.; Taud, H.; Marciano-Melchor, M.: Robust switched tracking control for wheeled mobile robots considering the actuators and drivers. Sensors **18**(12), 4316 (2018)

37. Levant, A.: Sliding order and sliding accuracy in sliding mode control. Int. J. Control **58**(6), 1247–1263 (1993)

38. Ouyang, H.; Hu, J.; Zhang, G.; Mei, L.; Deng, X.: Sliding-mode-based trajectory tracking and load sway suppression control for double-pendulum overhead cranes. IEEE Access **7**, 4371–4379 (2019)

39. Tuan, L.A.; Lee, S.: Sliding mode controls of double-pendulum crane systems. J. Mech. Sci. Technol. **27**, 1863–1873 (2013)

40. Ouyang, H.; Wang, J.; Zhang, G.; Mei, L.; Deng, X.: Novel adaptive hierarchical sliding mode control for trajectory tracking and load sway rejection in double-pendulum overhead cranes. IEEE Access **7**, 10353–10361 (2019)

41. Sun, N.; Fang, Y.; Chen, H.; Fu, Y.: Super-twisting-based antiswing control for underactuated double pendulum cranes. In: Proceedings of 2015 IEEE International Conference on Advanced Intelligent Mechatronics, Busan, July 76-11, pp. 749–754 (2015)

42. Sun, N.; Yang, T.; Fang, Y.; Wu, Y.; Chen, H.: Transportation control of double-pendulum cranes with a nonlinear quasi-PID scheme: design and experiments. IEEE Trans. Syst. Man Cybern. Syst. **49**(7), 1408–1418 (2019)

43. Sun, N.; Fang, Y.; Chen, H.; Lu, B.: Amplitude-Saturated nonlinear output feedback antiswing control for underactuated cranes with double-pendulum cargo dynamics. IEEE Trans. Ind. Electron. **64**, 2135–2146 (2017)

44. Sun, N.; Wu, Y.; Fang, Y.; Chen, H.: Nonlinear antiswing control for crane systems with double-pendulum swing effects and uncertain parameters: design and experiments. IEEE Trans. Autom. Sci. Eng. **15**(3), 1413–1422 (2018)

45. Zhang, M.; Ma, X.; Rong, X.; Song, R.; Tian, X.; Li, Y.: A novel energy-coupling-based control method for double-pendulum overhead cranes with initial control force constraint. Adv. Mech. Eng. **10**(1), 1–13 (2018)

46. Sun, N.; Wu, Y.; Chen, H.; Fang, Y.: An energy-optimal solution for transportation control of cranes with double pendulum dynamics: design and experiments. Mech. Syst. Signal Process. **102**, 87–101 (2018)

47. Lu, B.; Fang, Y.; Sun, N.: Enhanced-coupling adaptive control for double-pendulum overhead cranes with payload hoisting and lowering. Automatica **101**, 241–251 (2019)

48. Chen, H.; Sun, N.: Nonlinear control of underactuated systems subject to both actuated and unactuated state constraints with experimental verification. IEEE Trans. Ind. Electron. **6**(9), 7702–7714 (2020)

49. Jaafar, H.I.; Mohamed, Z.; Mohd Subha, N.A.; Husain, A.R.; Ismail, F.S.; Ramli, L.; Tokhi, M.O.; Shamsudin, M.A.: Efficient control of a nonlinear double-pendulum overhead crane with sensorless payload motion using an improved PSO-tuned PID controller. J. Vib. Control **25**(4), 907–921 (2019)

50. Aguilar-Ibáñez, C.; Suarez-Castanon, M.S.: A trajectory planning based controller to regulate an uncertain 3D overhead crane system. Int. J. Appl. Math. Comput. Sci. **29**(4), 693–702 (2019)

51. Jaafar, H.I.; Mohamed, Z.; Shamsudin, M.A.; Mohd Subha, N.A.; Ramli, L.; Abdullahi, A.M.: Model reference command shaping for vibration control of multimode flexible systems with application to a double-pendulum overhead crane. Mech. Syst. Signal Process. **115**, 677–695 (2019)

52. Jaafar, H.I., Mohamed, Z., Ramli, L.; Abdullahi, A.M.: Vibration control of a nonlinear double-pendulum overhead crane using feed-forward command shaping. In: Proceedings of 2018 IEEE Conf. Sys., Process and Control, Melaka, Malaysia, December 14–15, pp. 118–122 (2018)

53. Zhang, M.; Ma, X.; Chai, H.; Li, Y.: A novel online motion planning method for double-pendulum overhead cranes. Nonlinear Dyn. **85**(2), 1079–1090 (2016)

54. Liu, C.,Sun, B., Li, F.: Acceleration planning based anti-swing and position control for double-pendulum cranes. In: Proceedings of 2017 29th Chinese Control And Decision Conference, Chongqing, May 28–30, pp. 5671–5675 (2017)

55. Moreno, J.A.: On strict Lyapunov functions for some non-homogeneous super-twisting algorithms. J. Franklin Inst. **351**(4), 1902–1919 (2014)

56. Nagesh, I.; Edwards, C.: A multivariable super-twisting sliding mode approach. Automatica **50**(3), 984–988 (2014)

57. Amin, J.; Friedland, B.; Harnoy, A.: Implementation of a friction estimation and compensation technique. IEEE Control Syst. Mag. **17**(4), 71–76 (1997)

58. Makkar, C., Dixon, W.E., Sawyer, W.G., Hu, G.: A new continuously differentiable friction model for control systems design. In: Proceedings of 2005 IEEE/ASME International Conference on Advanced Intelligent Mechatronics, Monterey, CA, July 24–28, pp. 600–605 (2015)

59. Utkin, V., Shi, J.: Integral sliding mode in systems operating under uncertainty conditions. In: Proceedings of 35th IEEE Conference on Decision and Control, Kobe, Vol. 4, pp. 4591–4596, December 13-13 (1996)

60. Poznyak, A.S.: Advanced Mathematical Tools for Automatic Control Engineers. Elsevier, Amsterdam (2009)

61. Priyadarshi, N.; Padmanaban, S.; Bhaskar, M.S.; Blaabjerg, F.; Holm-Nielsen, J.B.; Azam, F.; Sharma, A.K.: A hybrid photovoltaic-fuel cell-based single-stage grid integration with lyapunov control scheme. IEEE Syst. J. **14**(3), 3334–3342 (2020)

62. Hiari, O.; Mesleh, R.; Al-Khatib, A.: A system simulation framework for modeling space modulation techniques. IEEE Syst. J. **14**(1), 1435–1446 (2020)